*Article*

# A Comparative Study of Cerium- and Ytterbium-Based GO/g-C$_3$N$_4$/Fe$_2$O$_3$ Composites for Electrochemical and Photocatalytic Applications

Nosheen Farooq [1,2], Rafael Luque [3], Mahmoud M. Hessien [4], Ashfaq Mahmood Qureshi [2], Farzana Sahiba [1], Muhammad Altaf Nazir [1] and Aziz ur Rehman [1,*]

1   Department of Chemistry, The Islamia University, Bahawalpur 63100, Pakistan;
    nosheen.farooq@gscwu.edu.pk (N.F.); sahibafarzana@gmail.com (F.S.); anch39@gmail.com (M.A.N.)
2   Department of Chemistry, The Government Sadiq College Women University, Bahawalpur 63100, Pakistan;
    ashfaq.qureshi@gscwu.edu.pk
3   Departamento de Quimica Organica, Campus de Rabanales, Edificio Marie Curie (C-3), Universidad de
    Cordoba, Ctra Nnal IV-A, Km 396, E14014 Cordoba, Spain; rafael.luque@uco.es
4   Department of Chemistry, College of Science, Taif University, P.O. Box 11099, Taif 21944, Saudi Arabia;
    m.hessien@tu.edu.sa
*   Correspondence: draziz@iub.edu.pk

**Abstract:** The design of sustainable and efficient materials for efficient energy storage and degradation of environmental pollutants (specifically organic dyes) is a matter of major interest these days. For this purpose, cerium- and ytterbium-based GO/g-C$_3$N$_4$/Fe$_2$O$_3$ composites have been synthesized to explore their properties, especially in charge storage devices such as supercapacitors, and also as photocatalysts for the degradation of carcinogenic dyes from the environment. Physicochemical studies have been carried out using XRD, FTIR, SEM, and BET techniques. Electrochemical techniques (cyclic voltammetry, galvanic charge discharge, and electrochemical impedance spectroscopy) have been employed to measure super-capacitance and EDLC properties. Results show that the gravimetric capacitance calculated from GCD results is 219 Fg$^{-1}$ for ytterbium- and 169 Fg$^{-1}$ for cerium-based nanocomposites at the current density of 1 A/g and scan rate of 2 mV/sec. The specific capacitance calculated for the ytterbium-based nanocomposite is 189 Fg$^{-1}$ as compared to 125 Fg$^{-1}$ for the cerium-based material. EIS results pointed to an enhanced resistance offered by cerium-based nanocomposites as compared to that of ytterbium, which can be assumed with the difference in particle size, as confirmed from structural studies including XRD. From obtained results, ytterbium oxide-based GO/g-C$_3$N$_4$/Fe$_2$O$_3$ is proven to be a better electro-catalyst as compared to cerium-based nanocomposites. Photocatalytic results are also in agreement with electrochemical results, as the degradation efficiency of ytterbium oxide-based GO/g-C$_3$N$_4$/Fe$_2$O$_3$ (67.11 and 83.50% for rhodamine B and methylene blue dyes) surpasses values observed for cerium-based GO/g-C$_3$N$_4$/Fe$_2$O$_3$ (63.08 and 70.61%).

**Keywords:** super capacitance; cerium oxide; ytterbium oxide; graphitic carbon nitride; photocatalytic degradation

## 1. Introduction

Owing to its versatile nature and multiple properties, including thermodynamic stability, high conductivity, speedy charge carrier mobility, larger surface area, and various functional groups at the surface, graphene oxide is one of the most favored forms of carbon that has been used in research for the past two decades. Using GO sheets as a substrate for anchoring various metal oxides is one of the most recent trends to provide maximum functionality regarding electrochemical, storage devising, and catalytic properties. Taking into account this scenario, GO has been used to anchor metal oxide nanoparticles [1,2].

The idea of using iron oxide ($Fe_2O_3$) nanoparticles for the preparation of composites is related to the transfer properties of $Fe_2O_3$ such as a good charge transfer mechanism regarding the average band gap, superior electrochemical energy storage, a non-toxic nature, and better chemical stability. GO has been used as a substrate to stabilize $Fe_2O_3$ nanoparticles that not only prevent the agglomeration but also refine the stacking factor of GO sheets [3]. Usui et al. efficiently synthesized $Fe_2O_3$/Sb using $\alpha$-$Fe_2O_3$ with Sb as an anode for Na-ion batteries [4].

Graphitic carbon nitride (g-$C_3N_4$) has attracted more attention from researchers due to its unique properties as a semiconductor with a 2.7 eV band gap in various photocatalytic applications. When g-$C_3N_4$ is combined with other conductive materials, its properties are enhanced toward various catalytic reactions [5].

In recent years, g-$C_3N_4$ has been utilized in supercapacitors due to its structure, good resistance properties, and presence of nitrogen. Three-dimensional graphene-based g-$C_3N_4$ electrodes have been developed in symmetric supercapacitors with a capacitance of 264 F $g^{-1}$ at 0.4 A $g^{-1}$ [6,7]. Asymmetric capacitors have remarkable electrochemical properties with high capacitance and current voltage as compared to symmetric supercapacitors. Ni $(OH)_2$-based g-$C_3N_4$ electrodes have been generated for asymmetric supercapacitors, having a capacitance of 505.6 F $g^{-1}$ at 0.5 A $g^{-1}$, with a low cyclic stability. $NiCo_2S_4$ nanosheet-based g-$C_3N_4$ has been developed to increase electrochemical properties, where capacitance is recorded as 506 C $g^{-1}$ at 1 A $g^{-1}$ [8–10].

A g-$C_3N_4$/CoS nanocomposite has been proposed for supercapacitors due to its enhanced capacitance of 668 F $g^{-1}$ at 2 A $g^{-1}$ [11]. The PANI/g-$C_3N_4$ nanocomposite exhibited an improved capacitance of 584.3 F $g^{-1}$ at 1 A $g^{-1}$, where electrodes gain high stability to make supercapacitors work more efficiently [12]. The development of the g-$C_3N_4$-based $Co_3O_4$ electrode rendered materials with a remarkable enhanced capacitance of 780 F $g^{-1}$ at 1.25 A $g^{-1}$ with a high cyclic stability [13].

The choice of cerium and ytterbium oxides to be a part of synthesized nanocomposites relates to their performance in redox processes to induce better capacitance properties and create improved band gap properties in order to carry out photocatalytic reactions. Studies indicate that Ce-$C_3N_4$ has been considered a versatile material due to its photocatalytic properties and high stability, with enhanced catalytic behavior in hydrogen evolution reactions [14]. F-doped Ce-$C_3N_4$ has been suggested for hydrogen energy production with enhanced photocatalytic properties. With a larger availability of active sites, Ce-$C_3N_4$ derivatives show enhanced catalytic activities in hydrogen reduction reactions [15]. H-$CeO_2$@GC has been developed by applying a coating of $CeO_2$ onto graphitic carbon that shows enhanced electrochemical activities with an increased surface area. The resulting material shows a specific capacitance of 501 F $g^{-1}$ at 1 A $g^{-1}$ with a high cyclic stability that makes it suitable for high performance supercapacitors [16]. Cerium and ytterbium oxides possess a larger surface area, uniform size, big band gap property, and better alignment of bands for transfer of charge carriers regarding electrochemical and photocatalytic activities [14,17].

The surface of graphitic carbon nitride has been utilized as support for anchorage of cerium and ytterbium oxide nanoparticles, respectively. In our work, cerium- and ytterbium-based nanocomposites have been synthesized using different precursors based on GO, graphitic carbon nitride, and iron oxide in order to compare their electrochemical behavior regarding charge storage as supercapacitors. Moreover, the photocatalytic activity regarding the removal of hazardous dyes (rhodamine B and methylene blue) from water has also been employed for a better comparison of applications in both types of materials.

## 2. Results and Discussion

FTIR results in Figure 1 can be described as, in the case of $CeO_2$ nanoparticles (Figure 1a), having a peak at 673 cm$^{-1}$ that corresponds to the stretching vibration of Ce-O group. The peak of 1290 cm$^{-1}$ being weak corresponds to Ce-OH overtone band, while the sharp peak at 1461 cm$^{-1}$ is assigned to the bending vibrations of C-H bond, and

the wide band at 3410 cm$^{-1}$ corresponds to stretching vibrations of O-H functional groups, respectively [18–20]. In Ce/GOCNIO NPs, the weaker peak at 1290 cm$^{-1}$ decreased, while all other peaks can be clearly seen in Figure 1c and d Considering Figure 1b for analyzing FTIR peaks of pure Yb$_2$O$_3$ nanoparticles, the peak at 618 cm$^{-1}$ is correlated to the stretching vibrations Yb-O-H, 1368 cm$^{-1}$ shows bending vibrations of C-O bonds, and 1621 cm$^{-1}$ is assigned to stretching mode of C-O vibrations, while the broad band at 3445 cm$^{-1}$ is due to O-H stretching vibrations, respectively [21–23]. In Yb/GOCNIO NPs, the intensity of the peak at 618 cm$^{-1}$ increased due to the intercalated Fe-O group within the nanocomposite structure [24], while the remaining three peaks are available with slight changes as shown in Figure 1d.
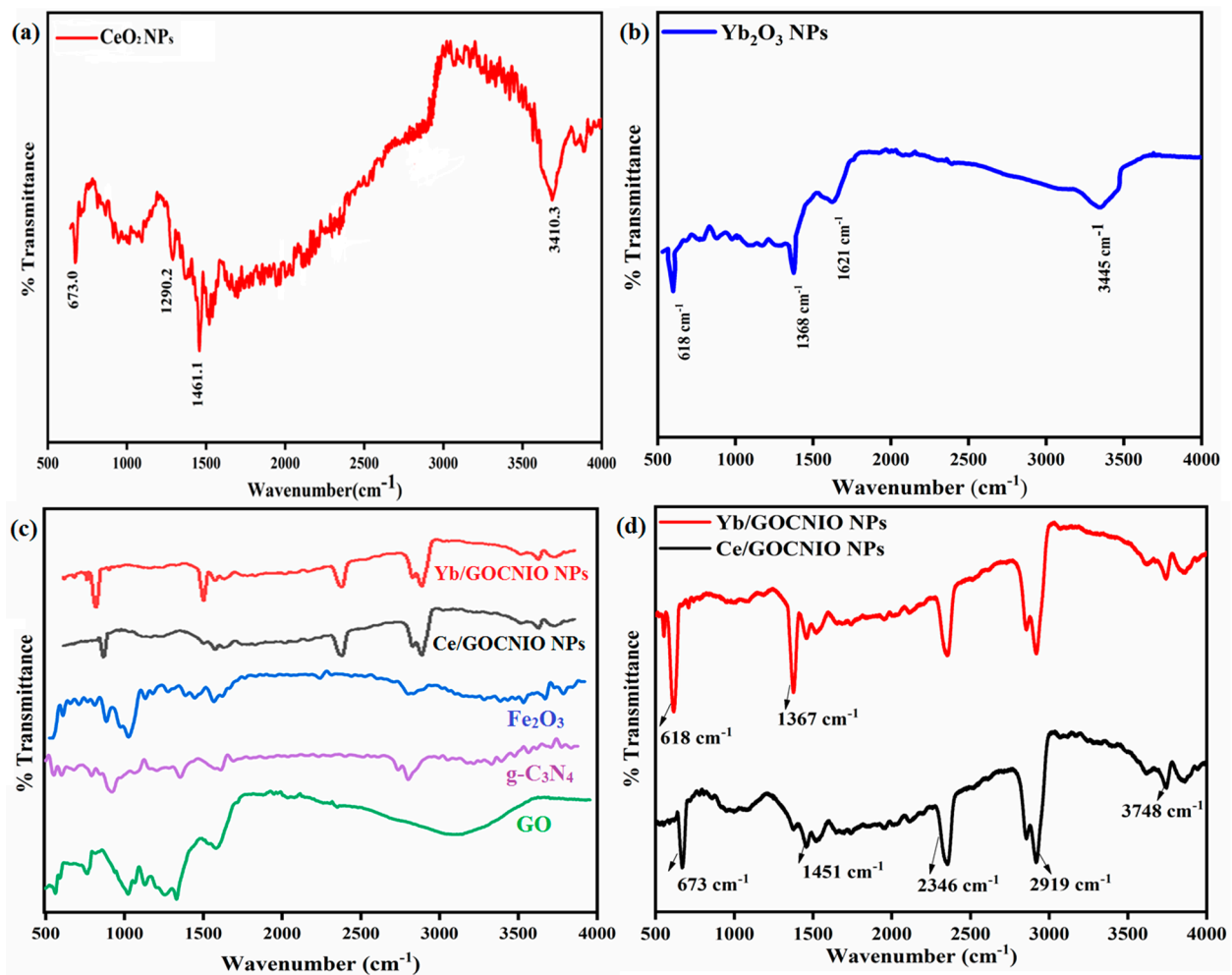


**Figure 1.** FTIR spectra of (**a**) CeO$_2$ NPs; (**b**) Yb$_2$O$_3$ NPs; (**c**) GO, g-C$_3$N$_4$, Fe$_2$O$_3$, Ce/GOCNIO NPs, and Yb/GOCNIO NPs; (**d**) Ce/GOCNIO NPs and Yb/GOCNIO NPs.

The peak of 1450 cm$^{-1}$ shows the reported range of stretching vibrations of the heterocyclic aromatic C-N linkage correlating the triazine rings of graphitic carbon nitride, respectively [25]. Common peaks in both nanocomposites are 2346 cm$^{-1}$, 2919 cm$^{-1}$, and 3748 cm$^{-1}$, respectively. All three of these peaks can be elucidated as significant peaks for C-C stretching, C-H stretching vibrations, and O-H stretching vibrations, respectively [26]. Moreover, peaks present in the range of 3500 cm$^{-1}$ to 3800 cm$^{-1}$ correspond to N-H functional groups of amino acids, confirming the presence of nanosheet-based graphitic carbon nitride as reported in the literature. There is a broadening of the peak area between 700 cm$^{-1}$ and 900 cm$^{-1}$ due to the presence of cerium and ytterbium nanoparticles, thus making small and weak the peaks for iron oxide onto graphene oxide sheets.

XRD patterns of pure $CeO_2$ NPs and $Yb_2O_3$ NPs are shown in Figure 2a,b, respectively. XRD patterns have been checked and confirmed using JCPDS card numbers of 01-081-0792 for $CeO_2$ NPs, and 00-018-0463 has been used for $Yb_2O_3$ NPs. Ce/GOCNIO NPs and Yb/GOCNIO NPs are depicted in Figure 2. The various diffraction peaks of Ce/GOCNIO NPs at 2-theta are of 10.7°, 19.6°, 27.8°, 32.9°, 35.5°, 47.9°, 54.1°, 57.3°, and 62.5°, indexed to planes (001), (113), (002), (200), (199), (220), (311), (428), and (203), respectively. The diffraction peaks at 2-theta of 19.6° and 27.8° could be attributed to g-$C_3N_4$ [27]. The characteristic diffraction peaks at 32.9°, 47.9°, and 54.1° were observed due to the presence of cerium oxide [19,28]. The crystallite size calculated from the Scherrer's formula $(D = K\lambda/(\beta \cos\theta))$ is 19 nm. The various diffraction peaks of Yb/GOCNIO NPs at 2-theta are of 10.7°, 19.6°, 22.0°, 27.8°, 29.6°, 35.5°, 57.3°, and 62.5°, indexed to planes (001), (113), (211), (002), (222), (119), (428), and (203), respectively. The characteristic diffraction peaks at 22.0° and 29.6° were observed due to the presence of ytterbium oxide [29–31]. The crystallite size for ytterbium ions was calculated to be 14 nm. The existence of only distinctive peaks and the absence of any other peak due to impurities in XRD patterns revealed the purity of as-prepared samples.
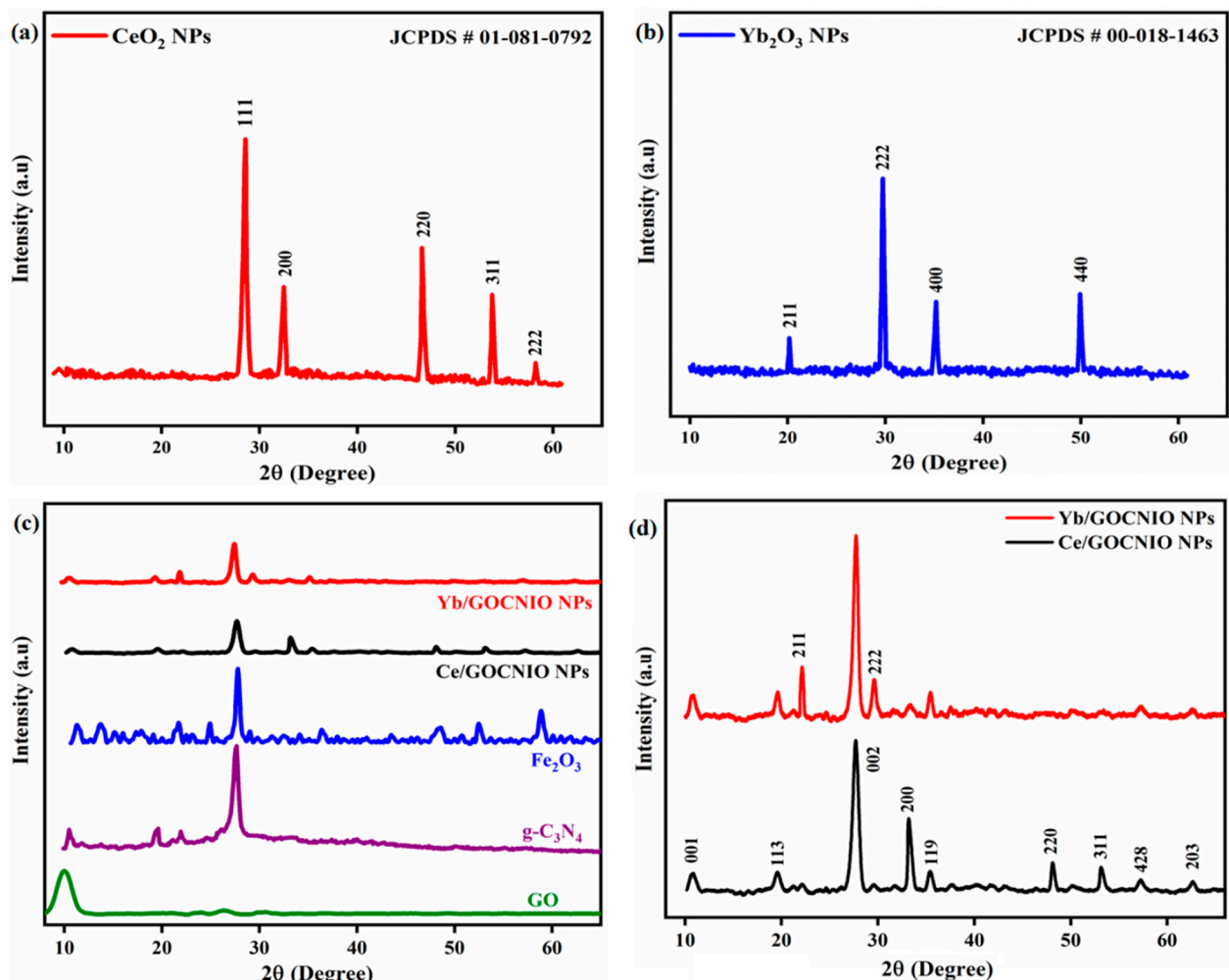


**Figure 2.** XRD patterns of (**a**) $CeO_2$ NPs; (**b**) $Yb_2O_3$ NPs; (**c**) GO, g-$C_3N_4$, $Fe_2O_3$, Ce/GOCNIO NPs, and Yb/GOCNIO NPs; (**d**) Ce/GOCNIO NPs; and Yb/GOCNIO NPs.

SEM images of nanocomposites are shown in Figure 3a,b, pointing to wrinkled and flaked frameworks comprised of graphitic carbon nitride along with adhered GO sheets bearing iron oxide nanoparticles. The nanoparticles available in the matrix can be attributed to the multi-phase structure where iron oxide grained particles are surrounded by whitish

shadows of cerium and ytterbium ions. The most probable arrangement is mentioned, as GO sheets act as adhering sites where iron oxide nanoparticles are being dispersed on layers along with attached graphitic carbon nitride flakes according to the available sites. Figure 3 depicts g-C$_3$N$_4$ flaked structures with dispersed prominent sized nanoparticles of cerium oxide and ytterbium oxide onto the surface of the flakes, with measured particle sizes (Figure 3). From results of XRD using Scherrer's equation, ca. 19 nm size (cerium oxide NPs) and ca. 14 nm size (ytterbium oxide nanoparticles) were respectively determined [32,33]. The nanocomposites formed are porous nano-architectures as confirmed from BET results, which provide a larger surface area and interfacial contact sites for a better charge transfer mechanism for better electrochemical and photocatalytic applications.
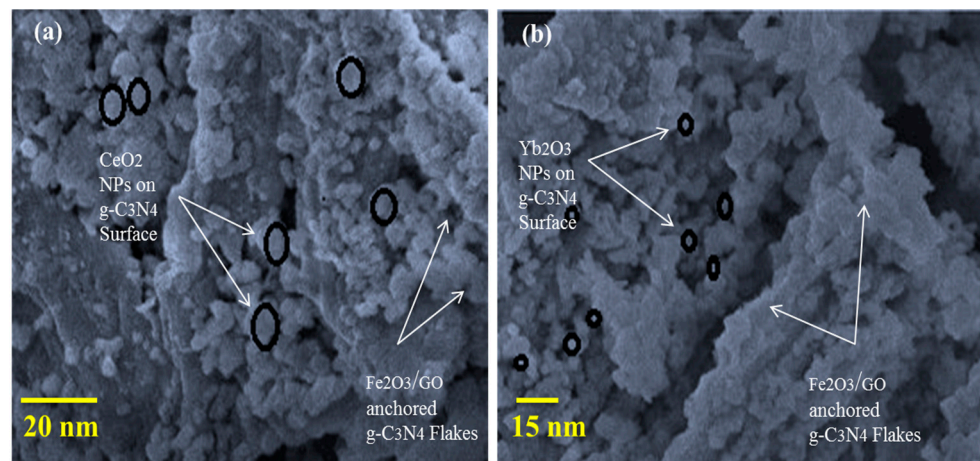


**Figure 3.** SEM images of (**a**) Ce/GOCN IONPs; (**b**) Yb/GOCN IONPs.

Cyclic voltammetry studies of prepared samples (Ce/GOCNIO NPs and Yb/GOCNIO NPs) were carried out in a 3 M KOH electrolyte using a nickel foam substrate. CV profiles of all samples were obtained in the potential window range from −0.65 V to 0.55 V at scan rates of 2, 5, 10, 20, 30, 40, and 50 mV/s. Figure 4a,b depicts CV profiles of Ce/GOCNIO NPs and Yb/GOCNIO NP electrodes, respectively. Figure 4a shows a quasi-rectangular shaped CV curve with diffused redox peaks, which shows both the faradaic and non-faradaic behavior to store the charge. The smaller area of the CV profile of the Ce/GOCNIO NPs electrode shows a poor charge storage proficiency [34,35]. The relatively larger enclosed area of the CV profile of Yb/GOCNIO NPs (Figure 4b) shows a better charge storage ability due to the highly conductive behavior of Yb in the nanocomposite of Yb/GOCNIO NPs. The specific capacitance of all the working electrodes was calculated using Equation (1):

$$Csp = \frac{A}{2\,\vartheta m \Delta V} \tag{1}$$

where 'Csp' represents the specific capacitance, A is the total area inside the CV-curve, $\Delta V$ is the potential window, 'm' is the active mass of the electrode material, and '$\vartheta$' is the scan rate.

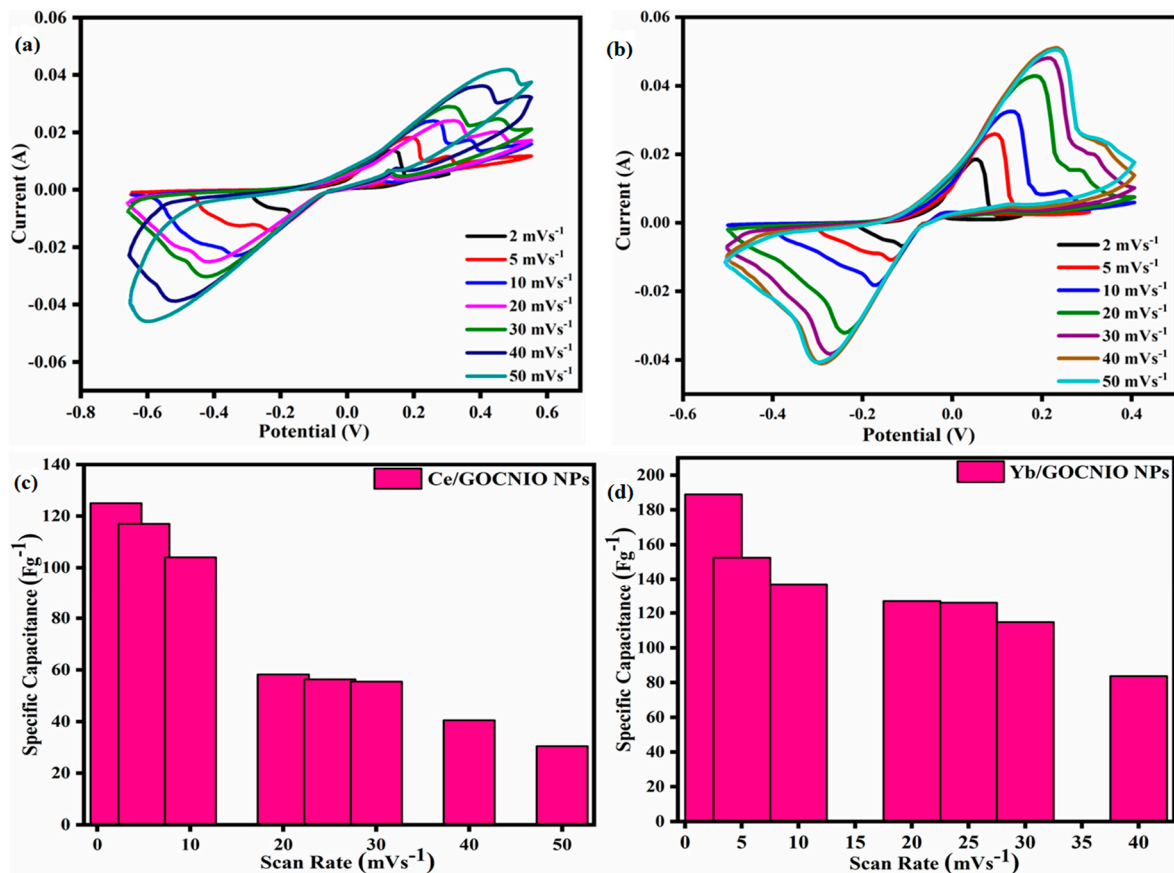**Figure 4.** (**a**) CV Profile of Ce/GOCNIO NPs; (**b**) CV Profile of Yb/GOCNIO NPs; (**c**) Influence of scan rates on specific capacitance of Ce/GOCNIO NPs; and (**d**) Influence of scan rates on specific capacitance of Yb/GOCNIO NPs.

The specific capacitance of Ce/GOCNIO NP electrodes at various scan rates such as 2, 5, 10, 20, 30, 40, and 50 mV/s was 125, 117, 104, 58.3, 55.5, 40.5, and 30.5 $Fg^{-1}$, respectively. Comparatively, Yb/GOCN IONPs electrodes exhibited a greater specific capacitance of 189.0 (maximum), 152.4, 136.9, 126.9, 125.9, 114.7, and 83.7 $Fg^{-1}$ at various scan rates such as 2, 5, 10, 20, 30, 40, and 50 mV/s, respectively, with respect to Ce/GOCNIO NPs electrodes. At a scan rate of 2 mV/s, Yb/GOCN IONPs exhibited the highest specific capacitance (189.0 $F\,g^{-1}$) as compared to Ce/GOCN IONPs (125 $F\,g^{-1}$) due to good charge storage capacity and a highly enclosed CV loop area [17].

Figure 4c,d shows the inverse effect of the scan rate on the specific capacitance of both working electrodes. As the scan rates increases, the specific capacitance of all the working electrodes decreases due to very short time interactions of working electrodes with electrolytes at higher scan rates [36].

Galvanic charge/discharge (GCD) profiles of both Ce/GOCNIO NP and Yb/GOCNIO NP electrodes at a current density of 1 A/g were subsequently recorded (Figure 5a). Yb/GOCNIO NPs exhibited an expanded and slightly triangular shape of GCD, which involved both faradaic and non-faradaic mechanisms for storing the charge [37].
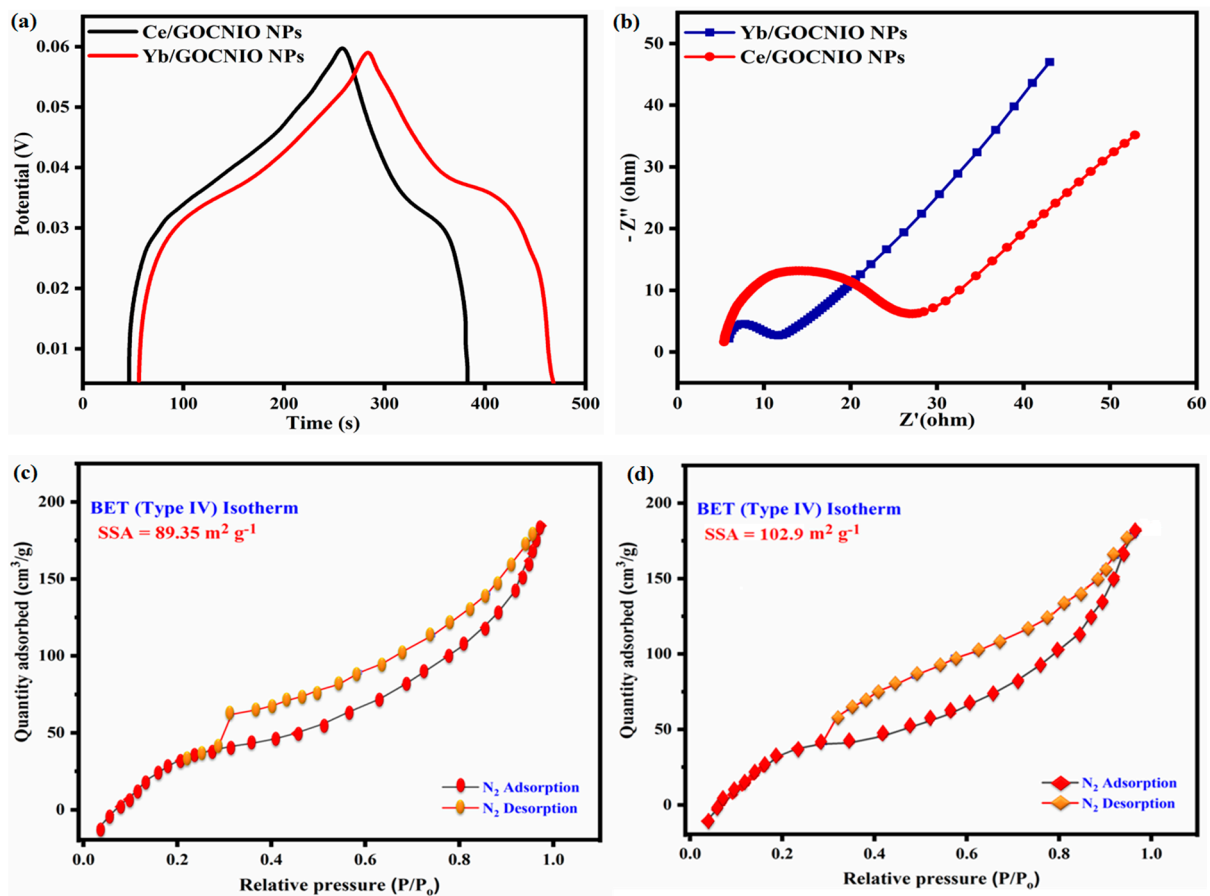
**Figure 5.** (**a**) GCD Profile of Ce/GOCNIO NPs and Yb/GOCNIO NPs; (**b**) EIS Nyquist Plots of Ce/GOCNIO NPs and Yb/GOCNIO NPs; (**c**) BET profile of Ce/GOCNIO NPs; (**d**) BET profile of Yb/GOCNIO NPs.

The gravimetric capacitance of all the electrodes was calculated using Equation (2):

$$Cg = i \times \Delta t \tag{2}$$

where 'i' is the current density, $\Delta t$ is the discharge time, and $\Delta V$ is the potential drop. The gravimetric capacitance of Yb/GOCNIO NPs was 219 $Fg^{-1}$ as compared to Ce/GOCNIO NPs (169 $Fg^{-1}$).

Electrochemical impedance spectroscopy (EIS) results provide information about various reaction resistances. The charge transfer resistance ($R_{ct}$) ascribes the diameter of the semicircled curve of impedance. EIS studies of prepared electrodes were conducted using an AC circuit. Results were obtained by using a 3M KOH electrolyte within the frequency range of 100 kHz to 100 mHz. The Nyquist plot of both Ce/GOCNIO NP and Yb/GOCNIO NP electrodes shows the non-vertical portion of the impedance plot taken at a lower frequency, which is observed due to an uneven pathway for the transport of electrolytic ions from the bulk electrolyte to the porous active surface of electrode, by the irregular distribution of pore size and coarseness of the electrode [38]. The larger diameter of the semicircled Ce/GOCNIO NPs shows a greater charge transfer resistance ($R_{ct}$) and possesses a larger value for Warburg resistance ($R_w$). In the case of Yb/GOCNIO NP electrodes, the curve possesses a very small semicircle and gives a lower $R_{ct}$ value. Yb/GOCNIO NPs also have a vertical impedance line at a low frequency, indicating the lowest Rw value and also representing EDLC behavior. Hence, the electrolyte's ions diffused quickly and improved the capacitance (Figure 5a).

For the confirmation of surface area and pore size, Brunauer Emmett Teller (BET) analysis was also conducted. Figure 5c,d indicate the nitrogen adsorption desorption

patterns of as-synthesized nanocomposites, being measured at $-196.03\ ^\circ$C in order to quantify the sorption of nitrogen contents. The hysteresis loop formed for Yb/GOCNIONPs showed a larger surface area of 103 m$^2$ g$^{-1}$ as compared to Ce/GOCNIONPs with a specific surface area of 89 m$^2$ g$^{-1}$, thus confirming the availability of enhanced surface area and porosity within the nanomaterial. A type IV BET hysteresis loop, classic for mesoporous 2-D nano-architectures, was observed in both nanocomposites as shown in Figure 5c,d.

The photocatalytic activity of cerium- and ytterbium-based nanocomposites was checked by using the rhodamine B and methylene blue dyes, respectively (Figure 6a–d). Dyes were prepared as 2.5 mg/250 mL using distilled water separately. The $\lambda_{max}$ of both dyes was first measured using a UV-visible spectrophotometer; MB dye showed a $\lambda_{max}$ of 665 nm and the RhB that of 554 nm [39,40]. A nanocomposite (5 mg) in a 500 mL dye solution was mixed and placed in the dark to attain equilibrium. After 2 h, the mixture was exposed to light under vigorous stirring. The time interval was set to 5 min for every reading in order to measure the percentage of degradation of RhB and MB repeatedly. Nearly 3 mL for each reading was used and showed a noticeable decrease in absorbance values, thus confirming the degradation of dyes [41,42].
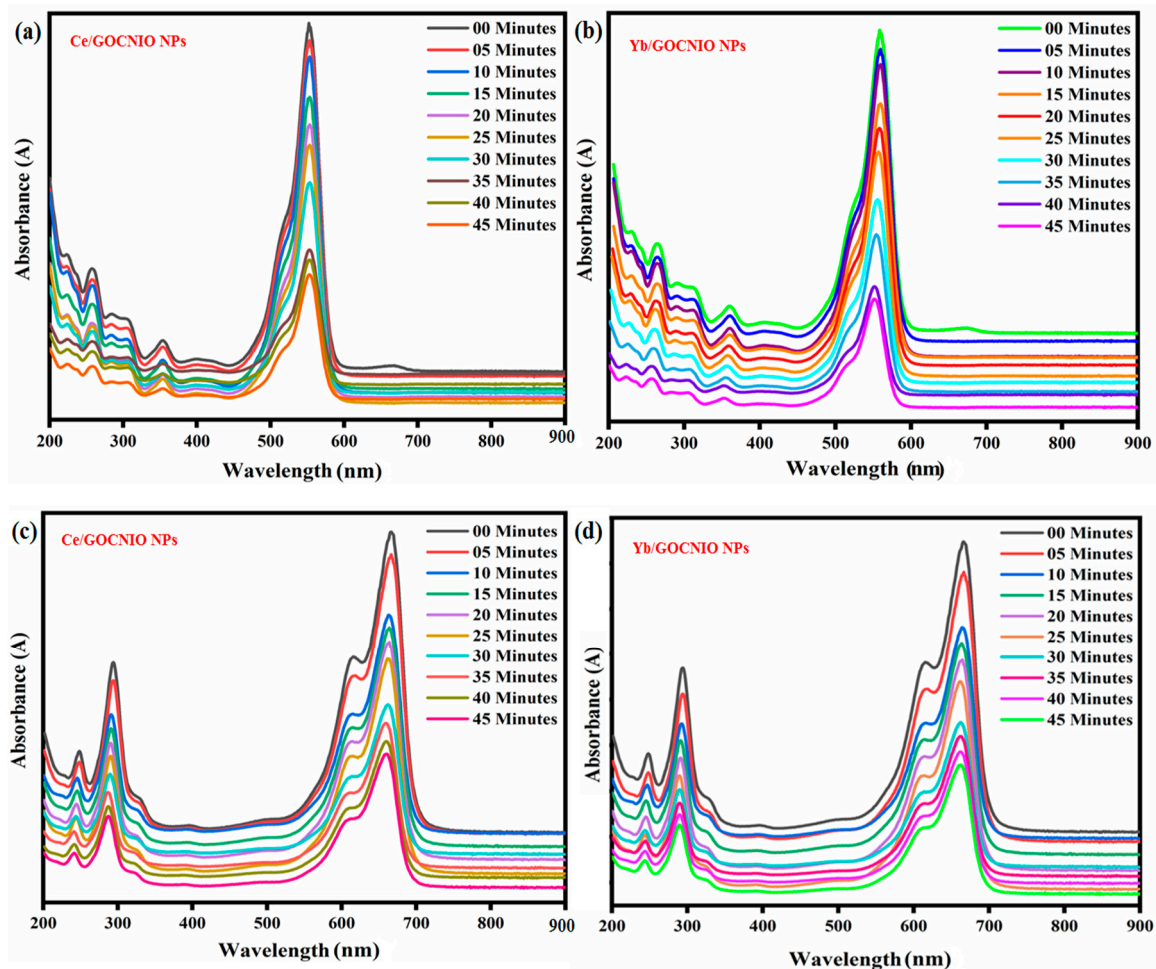


**Figure 6.** Percentage of degradation of RhB dye by (**a**) Ce/GOCNIO NPs, (**b**) Yb/GOCNIO NPs; Percentage degradation of MB dye by (**c**) Ce/GOCNIO NPs, (**d**) Yb/GOCNIO NPs.

The photocatalytic efficiency of the nanocomposites used has been worked out by using Equation (3) [43,44] as

$$\% \ D = \frac{[A_o - A_t]}{A_o} * 100 \tag{3}$$

where % D is the degradation in percentage, Ao is the initial absorbance taken at zero time, and At is the absorbance taken at time 't' when the sample was irradiated using a light bulb. Figure 7a,b represent the degradation efficiency of the synthesized photocatalysts.
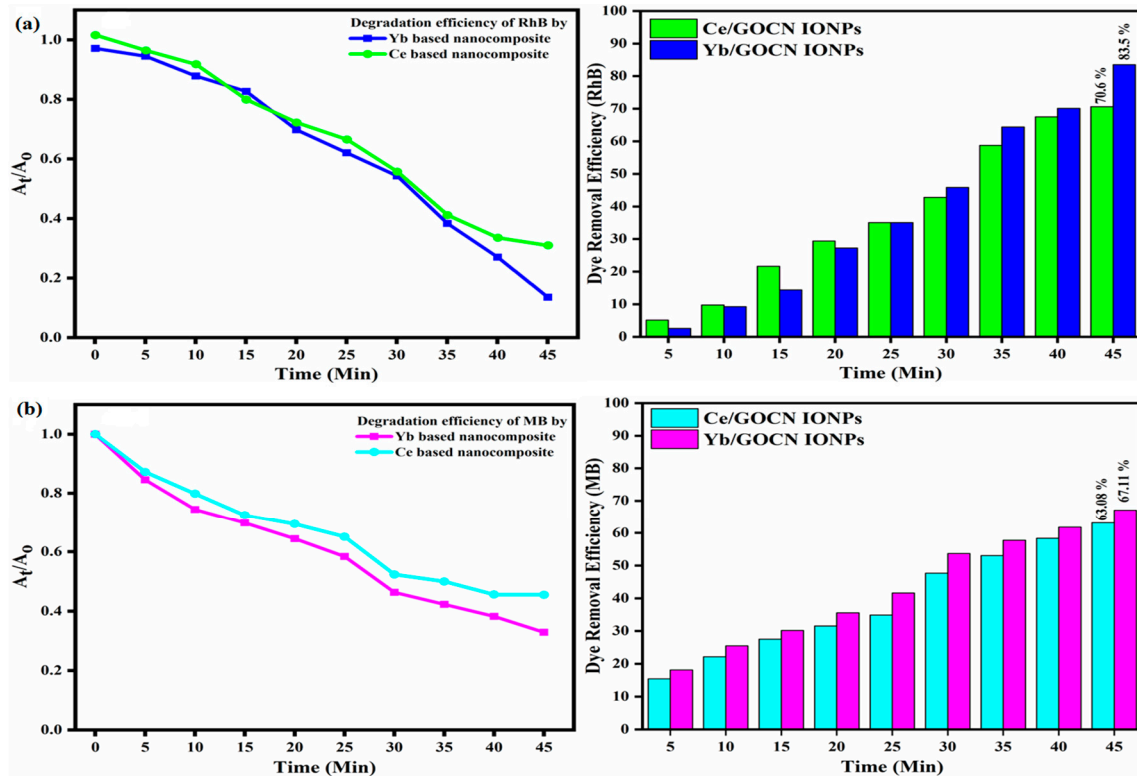


**Figure 7.** Efficiency comparison of (**a**) RhB dye and (**b**) MB dye by using Ce- and Yb-based nanocomposites.

For determining the transfer of charge carriers in semiconductors, the band edge potential can be calculated using well-known equations as

$$E_{CB} = X - \left(E_{ef} + 0.5\, E_g\right) \quad (4)$$

$$E_{VB} = E_{CB} + E_g \quad (5)$$

where X, $E_g$, $E_{CB}$, and $E_{VB}$ are the expressions of electro negativity, band gap, conduction band edge potential, and valence band edge potential, respectively, whereas Eef is the free e-energy relative to the H-scale (4.25 eV). The band gap for $Fe_2O_3$ is 2.3 eV and 2.7 eV for the graphitic carbon nitride material (Table 1), as both materials are key to establishing heterojunctions in nanocomposites for the photocatalytic degradation of dyes. From Figure 8, it is clear that the superoxide radical formation is actually the path for the degradation of dyes because of the high CB potential of $Fe_2O_3$, thus converting $O_2$ to superoxide radicals ($O_2$-*).

**Table 1.** Band gap values calculated for $g-C_3N_4$ and $Fe_2O_3$ semiconducting materials.

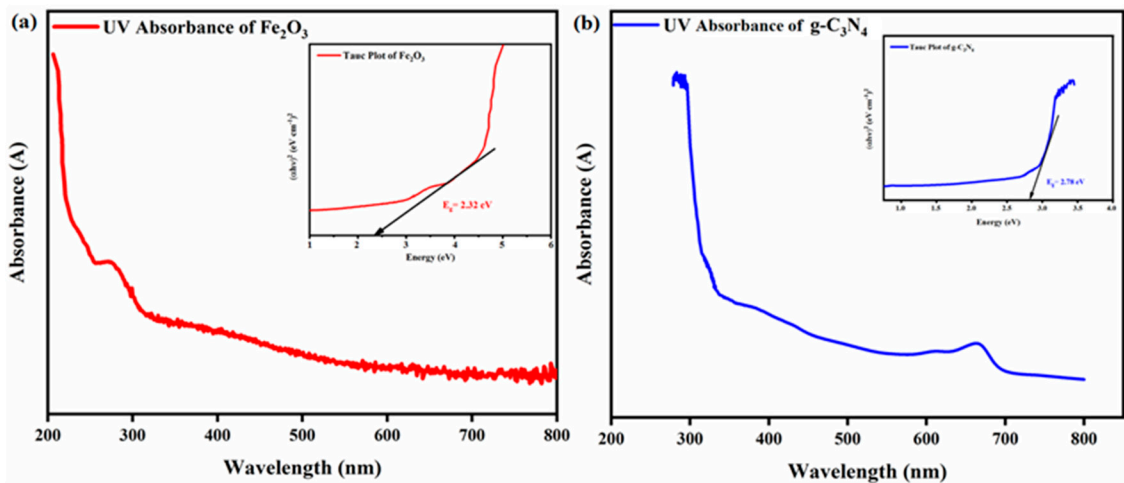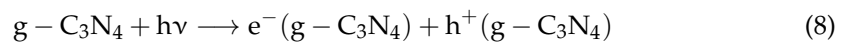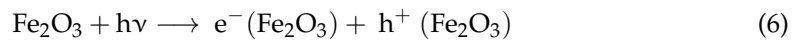| Material | Electro-Negativity (eV) | Band Gap (eV) | Valence Band Potential (eV) | Conduction Band Potential (eV) |
|---|---|---|---|---|
| $Fe_2O_3$ | 5.27 | 2.3 | 2.1 | −0.13 |
| $g-C_3N_4$ | 4.67 | 2.7 | 1.77 | −0.93 |

**Figure 8.** Possible band gaps calculated for (**a**) g-C3N4 and (**b**) Fe$_2$O$_3$ precursors.

The major reaction intermediates formed and their degradation activity involved can be expressed as

$$Fe_2O_3 + h\nu \longrightarrow e^- (Fe_2O_3) + h^+ (Fe_2O_3) \tag{6}$$

$$e^- (Fe_2O_3) + O_2 \longrightarrow O_2^{*-} \tag{7}$$

$$g - C_3N_4 + h\nu \longrightarrow e^- (g - C_3N_4) + h^+ (g - C_3N_4) \tag{8}$$

$$O_2^{*-} + Dye \longrightarrow Intermediates \tag{9}$$

Based on these points, the possible charge transfer mechanism is shown in Scheme 1.
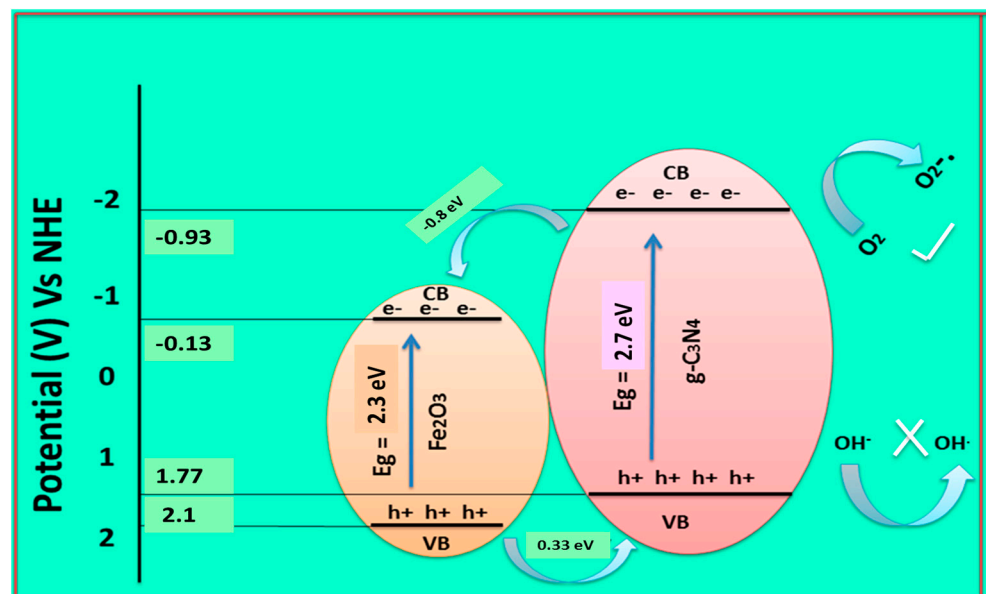


**Scheme 1.** Band structure and possible charge transport mechanism.

A comparison of photocatalytic efficiency was established between literature data as compared to the present results (Table 2). It is evident from the tabulated data that the designed nanocomposites are more effective and efficient as compared to a range of literature reported results for the photo-degradation of MB and RhB dyes.

**Table 2.** Comparative effectiveness of various photocatalysts in the photo-degradation of rhodamine B and methylene blue.

| Photocatalyst | Quantity (mg) | Dyes Used | Removal (%) | Time (Min) | Reference |
|---|---|---|---|---|---|
| $Fe_2O_3$@MgO | 0.1 | RhB/MB | 73/91 | 120 | [45] |
| Co-$Fe_3O_4$ | 25 | MB | 92 | 120 | [46] |
| $Fe_2O_3$/g-$C_3N_4$ | 1 | RhB | 90 | 120 | [47] |
| Ag-PMOS | 10 | MB | 81 | 60 | [48] |
| $CaPbFe_{12}O_{19}$ Composite | 50 | MB | 85 | 120 | [49] |
| ZnS/g-$C_3N_4$ | 5 | RhB | 90 | 90 | [50] |
| PVDF/g-$C_3N_4$ | 5 | RhB | 80 | 120 | [51] |
| $TiO_2$/g-$C_3N_4$ | 10 | RhB | 80 | 300 | [52] |
| $Yb_2O_3$/GOCNIONPs | 5 | RhB/MB | 67.11/83.5 | 45/45 | Current work |

## 3. Conclusions

Graphitic carbon nitride and its nanocomposites using cerium and ytterbium oxides were prepared by adopting exfoliation and co-precipitation methods. The synthesized nanocomposites possessed a layered and winkled morphology with an even distribution of nanoparticles as confirmed by SEM results. Yb/GOCN IONPs exhibited a high gravimetric capacitance with 219 $Fg^{-1}$ as compared to 169 $Fg^{-1}$ exhibited by Ce/GOCN IONPs. The EIS Nyquist plot possessed a very small semicircle and gave lower Rct and Rw values as compared to Ce/GOCN IONPs. These facts proved fruitful for nominating Yb/GOCN IONPs as a better candidate regarding electrochemical applications. Potential results for the photocatalytic degradation of dyes regarding RhB/MB with 67.11%/83.50% were obtained by Yb/GOCN IONPs in a minimum amount of time as compared to Ce/GOCNIO NPs, thus proving a better and promising catalyst in the field of the photocatalytic degradation of dyes. Yb/GOCNIO NPs are considered as a promising candidate capable of potential electrochemical and photocatalytic applications. The present work proves to be an efficient attempt at synthesizing a promising bifunctional catalyst for energy storage purposes as well as for the degradation of dangerous dyes in the environment.

## 4. Experimental

### 4.1. Materials Used

The chemicals used for this work were all of analytical grade, and no further purification was needed before usage. Major chemicals used are listed as graphite powder (99% pure), hydrogen peroxide ($H_2O_2$) (Merck, Darmstadt, Germany), potassium permanganate ($KMNO_4$) (Merck, Darmstadt, Germany), sulfuric acid ($H_2SO_4$) (Merck, Darmstadt, Germany), ethanol (Merck Germany), hydrochloric acid (HCl, Merck Germany), sodium hydroxide (NaOH) (Sigma Aldrich, Saint Louis, MO, USA), potassium hydroxide (KOH) (Sigma Aldrich, Saint Louis, MO, USA), ferrous sulphate heptahydrate ($FeSO_4 \cdot 7H_2O$) (Sigma Aldrich, Saint Louis, MO, USA), polyethylene glycol (PEG) (Sigma Aldrich, Saint Louis, MO, USA), cetyl trimethyl ammonium bromide (CTAB) (Sigma Aldrich, Saint Louis, MO, USA), urea ($CH_4N_2O$) (Sigma Aldrich, Saint Louis, MO, USA), cerium nitrate hexahydrate ($Ce(NO_3)_2 \cdot 6H_2O$, ytterbium nitrate pentahydrate ($Yb(NO_3)_3 \cdot 5H_2O$), nickel foam, nafion (binder), and distilled and deionized water for solution preparation and washing.

### 4.2. Synthesis of GO, $Fe_2O_3$, and $Fe_2O_3$/GO Nano-Composite

Graphene oxide was the first precursor prepared by following modified hummer's method [53]. The $Fe_2O_3$ nanoparticles were prepared by co-precipitation. A 0.6 molar NaOH solution was dropwisely added with constant stirring to 0.1 molar ferrous sulphate until pH 9 was adjusted, followed by addition of 1% PEG aqueous solution and 1% CTAB to ensure stable iron oxide nanoparticle formation. The mixture was stirred at 110 °C. After four hours, black colored product was obtained. The mixture was cooled to normal

temperature, and the product was washed thoroughly many times with distilled water to remove extra base. $Fe_2O_3$ nanoparticles were dried at 90 °C using oven to evaporate the solvent [54]. $GO/Fe_2O_3$ (1:2) nanocomposite was prepared by dispersing GO in distilled water with sonication for 30 min, followed by addition of $Fe_2O_3$ nanoparticles. The process of ultrasonication was continued for 1 h, and the final product was dried in vacuum oven till complete removal of water contents.

### 4.3. Synthesis of Carbon Nitride (g-$C_3N_4$) and GOCN IONPs

Thermal exfoliation method has been used for preparation of graphitic carbon nitride precursor. First, about 20 g of urea was put in alumina crucible, which was covered with lid and placed in muffle furnace heated at 550 °C for 4.5 h. The yellowish graphitic carbon nitride (g-$C_3N_4$) was obtained in the form of amorphous flakes, which was cooled to room temperature followed by grinding using mortar and pestle [55].
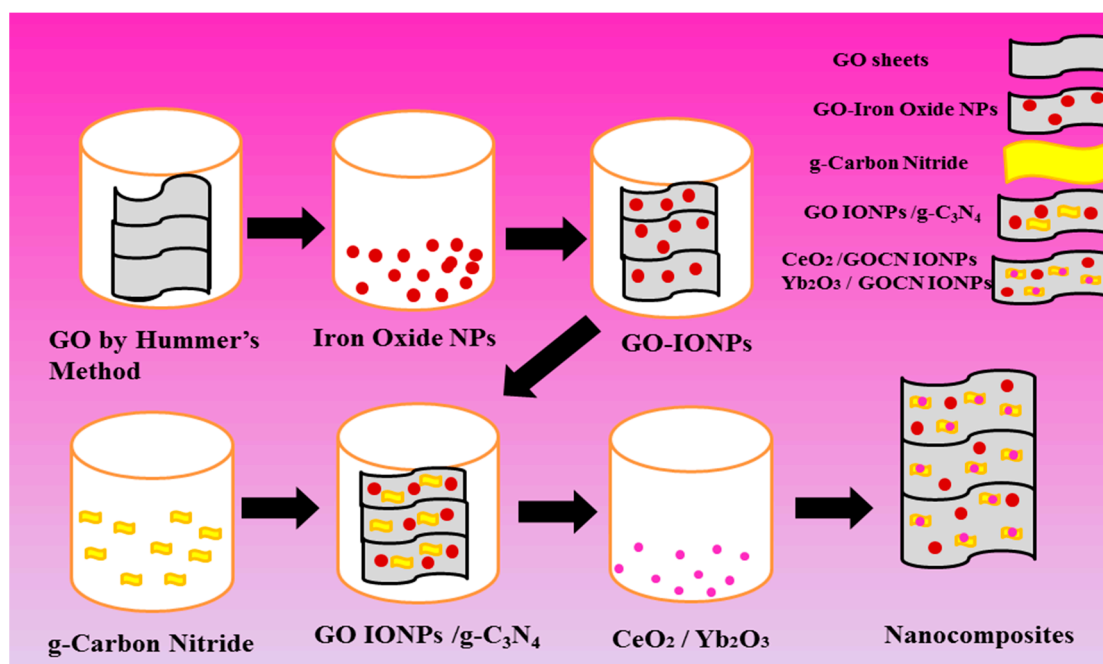
The nanocomposite was prepared by an effort of combining graphitic carbon nitride flakes possessing positive charge, with iron oxide anchored graphene oxide being negatively charged, in order to prepare the GO IONPs/g-$C_3N_4$ composite. For this preparation, separate solutions were prepared by dispersing g-$C_3N_4$ in 0.001 molar HCl along with sonication; similarly, graphene oxide bearing iron oxide was dispersed in 0.001 molar HCl solutions with sonication. Both solutions were sonicated at pH 3. The mixing through sonication was continued to 1.5 h. After that, the grayish yellow powdered product obtained was completely dried at 70 °C [56].

### 4.4. Synthesis of $CeO_2$ and $Yb_2O_3$ Nanoparticles

Cerium oxide and ytterbium oxide nanoparticles were prepared separately by simply using co-precipitation method. For this purpose, initially 0.08 g of NaOH was taken to prepare 0.1 molar solution using distilled water. Then, 0.5 molar solutions of cerium nitrate and ytterbium nitrate were prepared in distilled water separately, and dropwise addition of base was ensured along with continuous mixing and stirring for about 25 min. After complete mixing, solutions were centrifuged and then washed many times with ethanol and distilled water. The products in the form of precipitates obtained were annealed at 110 °C for half an hour. The resultant powders obtained were $CeO_2$ and $Yb_2O_3$, respectively [19].

### 4.5. Synthesis of $CeO_2$/GOCN IONPs and $Yb_2O_3$/GOCN IONPs

An effort was made to prepare Ce/GOCN IONPs and Yb/GOCN IONPs as final products (Scheme 2). For this, equal amounts of graphene oxide graphitic carbon nitride iron oxide composite were taken in separate beakers to disperse them in 15 mL distilled water with ultrasonication. Cerium and ytterbium nanoparticles (0.5 mg each), were dissolved in alcohol/water mixture solvent to prepare colloidal solutions followed by constant sonication for half an hour. The final product obtained was dried at 100 °C, and powdered form was obtained using mortar and pestle.

**Scheme 2.** Pictorial illustration for the synthesis of Ce/GOCN IONPs and Yb/GOCN IONPS.

## References

1. Wang, Z.; Liu, C.-J. Preparation and application of iron oxide/graphene based composites for electrochemical energy storage and energy conversion devices: Current status and perspective. *Nano Energy* **2015**, *11*, 277–293. [CrossRef]
2. Singh, V.; Patra, M.; Manoth, M.; Gowd, G.; Vadera, S.; Kumar, N. In situ synthesis of graphene oxide and its composites with iron oxide. *New Carbon Mater.* **2009**, *24*, 147–152. [CrossRef]
3. Zhu, Y.; Murali, S.; Cai, W.; Li, X.; Suk, J.W.; Potts, J.R.; Ruoff, R.S. Graphene and graphene oxide: Synthesis, properties, and applications. *Adv. Mater.* **2010**, *22*, 3906–3924. [CrossRef]
4. Usui, H.; Domi, Y.; Iwama, E.; Kurokawa, H.; Sakaguchi, H. $\alpha$-Fe$_2$O$_3$ conversion anodes with improved Na-Storage properties by Sb addition. *Mater. Chem. Phys.* **2021**, *272*, 125023. [CrossRef]
5. Choi, D.S.; Lee, H.; Tieves, F.; Lee, Y.W.; Son, E.J.; Zhang, W.; Shin, B.; Hollmann, F.; Park, C.B. Bias-Free In Situ H$_2$O$_2$ Generation in a Photovoltaic-Photoelectrochemical Tandem Cell for Biocatalytic Oxyfunctionalization. *ACS Catal.* **2019**, *9*, 10562–10566. [CrossRef]
6. Sanati, S.; Rezvani, Z. g-C$_3$N$_4$ nanosheet@ CoAl-layered double hydroxide composites for electrochemical energy storage in supercapacitors. *Chem. Eng. J.* **2019**, *362*, 743–757. [CrossRef]
7. Joseph, N.; Bose, A.C. Metallic MoS$_2$ grown on porous g-C$_3$N$_4$ as an efficient electrode material for supercapattery application. *Electrochim. Acta* **2019**, *301*, 401–410. [CrossRef]

8.    Kaipannan, S.; Marappan, S. Fabrication of 9.6 V high-performance asymmetric supercapacitors stack based on nickel hexacyanoferrate-derived Ni(OH)$_2$ nanosheets and bio-derived activated carbon. *Sci. Rep.* **2019**, *9*, 1–14. [CrossRef]

9.    Le, K.; Gao, M.; Liu, J.; Wang, Z.; Wang, F.; Murugadoss, V.; Wu, S.; Ding, T.; Guo, Z. MOF-derived hierarchical core-shell hollow iron-cobalt sulfides nanoarrays on Ni foam with enhanced electrochemical properties for high energy density asymmetric supercapacitors. *Electrochim. Acta* **2019**, *323*, 134826. [CrossRef]

10.   Hussain, S.; Javed, M.S.; Asimd, S.; Shaheen, A.; Khan, A.J.; Abbas, Y.; Ullah, N.; Iqbal, A.; Wang, M.; Qiao, G.; et al. Novel gravel-like NiMoO$_4$ nanoparticles on carbon cloth for outstanding supercapacitor applications. *Ceram. Int.* **2020**, *46*, 6406–6412. [CrossRef]

11.   Mohammadi, A.; Arsalani, N.; Tabrizi, A.G.; Moosavifard, S.E.; Naqshbandi, Z.; Ghadimi, L.S. Engineering rGO-CNT wrapped Co3S4 nanocomposites for high-performance asymmetric supercapacitors. *Chem. Eng. J.* **2018**, *334*, 66–80. [CrossRef]

12.   Zhou, S.-X.; Tao, X.-Y.; Ma, J.; Guo, L.-T.; Zhu, Y.-B.; Fan, H.-L.; Liu, Z.-S.; Wei, X.-Y. Synthesis of flower-like PANI/g-C$_3$N$_4$ nanocomposite as supercapacitor electrode. *Vacuum* **2018**, *149*, 175–179. [CrossRef]

13.   Wu, J.; Huang, Y.; Ye, W.; Li, Y. CO$_2$ reduction: From the electrochemical to photochemical approach. *Adv. Sci.* **2017**, *4*, 1700194. [CrossRef]

14.   Humayun, M.; Hu, Z.; Khan, A.; Cheng, W.; Yuan, Y.; Zheng, Z.; Fu, Q.; Luo, W. Highly efficient degradation of 2,4-dichlorophenol over CeO$_2$/g-C$_3$N$_4$ composites under visible-light irradiation: Detailed reaction pathway and mechanism. *J. Hazard. Mater.* **2019**, *364*, 635–644. [CrossRef]

15.   Zhang, L.; Jin, Z.; Huang, S.; Zhang, Y.; Zhang, M.; Zeng, Y.-J.; Ruan, S. Ce-Doped Graphitic Carbon Nitride Derived from Metal Organic Frameworks as a Visible Light-Responsive Photocatalyst for H$_2$ Production. *Nanomaterials* **2019**, *9*, 1539. [CrossRef] [PubMed]

16.   Wu, W.; Qi, W.; Zhao, Y.; Tang, X.; Qiu, Y.; Su, D.; Fan, H.; Wang, G. Hollow CeO$_2$ spheres conformally coated with graphitic carbon for high-performance supercapacitor electrodes. *Appl. Surf. Sci.* **2019**, *463*, 244–252. [CrossRef]

17.   Farbod, F.; Mazloum-Ardakani, M.; Naderi, H.R.; Mohammadian-Sarcheshmeh, H. Synthesis of a porous interconnected nitrogen-doped graphene aerogel matrix incorporated with ytterbium oxide nanoparticles and its application in superior symmetric supercapacitors. *Electrochim. Acta* **2019**, *306*, 480–488. [CrossRef]

18.   Coates, J. Interpretation of infrared spectra, a practical approach. In *Encyclopedia of Analytical Chemistry: Applications, Theory and Instrumentation*; John Wiley & Sons: Hoboken, NJ, USA, 2006.

19.   Pujar, M.S.; Hunagund, S.M.; Desai, V.R.; Patil, S.; Sidarai, A.H. One-step synthesis and characterizations of cerium oxide nanoparticles in an ambient temperature via Co-precipitation method. *Conf. Proc.* **2018**, *1942*, 050026.

20.   Farahmandjou, M.; Zarinkamar, M.; Firoozabadi, T. Synthesis of Cerium Oxide (CeO$_2$) nanoparticles using simple CO-precipitation method. *Rev. Mex. Física* **2016**, *62*, 496–499.

21.   Sun, Y.-H.; Yang, Z.-M.; Xie, C.-N.; Jiang, Z.-H. Comparative Study of Synthesis and Characterization of YAG: Yb3+ Nanoparticles Using Different Precipitator by Co-Precipitation Method. *J. Nanosci. Nanotechnol.* **2010**, *10*, 8102–8111. [CrossRef]

22.   Unal, F.; Kaya, F. Modelling of relation between synthesis parameters and average crystallite size of Yb$_2$O$_3$ nanoparticles using Box-Behnken design. *Ceram. Int.* **2020**, *46*, 26800–26808. [CrossRef]

23.   Naderi, H.R.; Ganjali, M.R.; Dezfuli, A.S.; Norouzi, P. Sonochemical preparation of a ytterbium oxide/reduced graphene oxide nanocomposite for supercapacitors with enhanced capacitive performance. *RSC Adv.* **2016**, *6*, 51211–51220. [CrossRef]

24.   Abdulah, H.I.; Farhan, A.M.; Ali, A.J. Photo-synthesis of nanosized α–Fe$_2$O$_3$. *J. Chem. Pharm. Res.* **2015**, *7*, 588–591.

25.   Chen, Y.; Liu, X.; Hou, L.; Guo, X.; Fu, R.; Sun, J. Construction of covalent bonding oxygen-doped carbon nitride/graphitic carbon nitride Z-scheme heterojunction for enhanced visible-light-driven H$_2$ evolution. *Chem. Eng. J.* **2020**, *383*, 123132. [CrossRef]

26.   Aleksandrzak, M.; Kukulka, W.; Mijowska, E. Graphitic carbon nitride/graphene oxide/reduced graphene oxide nanocomposites for photoluminescence and photocatalysis. *Appl. Surf. Sci.* **2017**, *398*, 56–62. [CrossRef]

27.   Baig, U.; Khan, A.; Gondal, M.A.; Dastageer, M.A.; Falath, W.S. Laser induced anchoring of nickel oxide nanoparticles on polymeric graphitic carbon nitride sheets using pulsed laser ablation for efficient water splitting under visible light. *Nanomaterials* **2020**, *10*, 1098. [CrossRef]

28.   Venkateswarlu, K.; Bose, A.C.; Rameshbabu, N. X-ray peak broadening studies of nanocrystalline hydroxyapatite by Williamson–Hall analysis. *Phys. B Condens. Matter* **2010**, *405*, 4256–4261. [CrossRef]

29.   Hosokawa, S.; Iwamoto, S.; Inoue, M. Synthesis of Mesoporous Needle-Shaped Ytterbium Oxide Crystals by Solvothermal Treatment of Ytterbium Chloride. *J. Am. Ceram. Soc.* **2007**, *90*, 1215–1221. [CrossRef]

30.   Bosund, M.; Mizohata, K.; Hakkarainen, T.; Putkonen, M.; Söderlund, M.; Honkanen, S.; Lipsanen, H. Atomic layer deposition of ytterbium oxide using β-diketonate and ozone precursors. *Appl. Surf. Sci.* **2009**, *256*, 847–851. [CrossRef]

31.   Dakhel, A. Annealing effect on the structural, optical and electrical properties of Yb–Mn oxide thin films. *J. Alloys Compd.* **2009**, *476*, 28–32. [CrossRef]

32.   Dezfuli, A.S.; Ganjali, M.R.; Norouzi, P.; Faridbod, F. Facile sonochemical synthesis and electrochemical investigation of ceria/graphene nanocomposites. *J. Mater. Chem. B* **2015**, *3*, 2362–2370. [CrossRef]

33.   Prabaharan, D.M.D.M.; Sadaiyandi, K.; Mahendran, M.; Sagadevan, S. Structural, optical, morphological and dielectric properties of cerium oxide nanoparticles. *Mater. Res.* **2016**, *19*, 478–482. [CrossRef]

34.   Kalubarme, R.S.; Kim, Y.-H.; Park, C.-J. One step hydrothermal synthesis of a carbon nanotube/cerium oxide nanocomposite and its electrochemical properties. *Nanotechnology* **2013**, *24*, 365401. [CrossRef] [PubMed]

35. Cui, K.-P.; Dai, R.-R.; Liu, X.; Weerasooriya, R.; Hong, Z.-Y.; Chen, X.; Wu, Y.-C. New strategy for fabricating Cd (II) sensing electrochemical interface based on enhanced adsorption followed by redox processes: Ferro-cerium oxide nanocomposite as an example. *J. Alloys Compd.* **2020**, *829*, 154551. [CrossRef]

36. Sabeeh, H.; Zulfiqar, S.; Aadil, M.; Shahid, M.; Shakir, I.; Khan, M.A.; Warsi, M.F. Flake-like $MoS_2$ nano-architecture and its nanocomposite with reduced Graphene Oxide for hybrid supercapacitors applications. *Ceram. Int.* **2020**, *46*, 21064–21072. [CrossRef]

37. Aghazadeh, M. Cathodic electrochemical deposition of nanostructured metal oxides/hydroxides and their composites for supercapacitor applications: A review. *Anal. Bioanal. Electrochem* **2019**, *11*, 211–266.

38. Yadav, N.; Singh, M.K.; Yadav, N.; Hashmi, S.A. High performance quasi-solid-state supercapacitors with peanut-shell-derived porous carbon. *J. Power Sources* **2018**, *402*, 133–146. [CrossRef]

39. Nazir, M.A.; Bashir, M.S.; Jamshaid, M.; Anum, A.; Najam, T.; Shahzad, K.; Imran, M.; Shah, S.S.A.; Rehman, A.U. Synthesis of porous secondary metal-doped MOFs for removal of Rhodamine B from water: Role of secondary metal on efficiency and kinetics. *Surf. Interfaces* **2021**, *25*, 101261. [CrossRef]

40. Farooq, N.; ur Rehman, A.; Qureshi, A.M.; ur Rehman, Z.; Ahmad, A.; Aslam, M.K.; Javed, H.M.A.; Hussain, S.; Habila, M.A.; AlMasoud, N. Au@ GO@ g-$C_3N_4$ and $Fe_2O_3$ nanocomposite for efficient photocatalytic and electrochemical applications. *Surf. Interfaces* **2021**, *26*, 101399. [CrossRef]

41. Liu, Y.; Wang, L.; Xue, N.; Wang, P.; Pei, M.; Guo, W. Ultra-Highly Efficient Removal of Methylene Blue Based on Graphene Oxide/TiO2/Bentonite Sponge. *Materials* **2020**, *13*, 824. [CrossRef]

42. Hernández-Uresti, D.; Vázquez, A.; Sanchez-Martinez, D.; Obregón, S. Performance of the polymeric g-$C_3N_4$ photocatalyst through the degradation of pharmaceutical pollutants under UV–vis irradiation. *J. Photochem. Photobiol. A Chem.* **2016**, *324*, 47–52. [CrossRef]

43. Monga, D.; Basu, S. Enhanced photocatalytic degradation of industrial dye by g-$C_3N_4$/$TiO_2$ nanocomposite: Role of shape of $TiO_2$. *Adv. Powder Technol.* **2019**, *30*, 1089–1098. [CrossRef]

44. Al-Rawashdeh, N.A.; Allabadi, O.; Aljarrah, M.T. Photocatalytic activity of graphene oxide/zinc oxide nanocomposites with embedded metal nanoparticles for the degradation of organic dyes. *ACS Omega* **2020**, *5*, 28046–28055. [CrossRef] [PubMed]

45. Venkatachalam, A.; Mark, J.A.M.; Deivatamil, D.; Revathi, J.; Prince Jesuraj, J. Sunlight active photocatalytic studies of $Fe_2O_3$ based nanocomposites developed via two-pot synthesis technique. *Inorg. Chem. Commun.* **2021**, *124*, 108417. [CrossRef]

46. Keerthana, S.; Yuvakkumar, R.; Ravi, G.; Kumar, P.; Elshikh, M.S.; Alkhamis, H.H.; Alrefaei, A.F.; Velauthapillai, D. A strategy to enhance the photocatalytic efficiency of α-$Fe_2O_3$. *Chemosphere* **2021**, *270*, 129498. [CrossRef]

47. Zhang, H.; Zhu, C.; Cao, J.; Tang, Q.; Li, M.; Kang, P.; Shi, C.; Ma, M. Ultrasonic-assisted synthesis of 2D α-$Fe_2O_3$@ g-$C_3N_4$ composite with excellent visible light photocatalytic activity. *Catalysts* **2018**, *8*, 457. [CrossRef]

48. Shahzad, K.; Najam, T.; Bashir, M.S.; Nazir, M.A.; Rehman, A.U.; Bashir, M.A.; Shah, S.S.A. Fabrication of Periodic Mesoporous Organo Silicate (PMOS) composites of Ag and ZnO: Photo-catalytic degradation of methylene blue and methyl orange. *Inorg. Chem. Commun.* **2021**, *123*, 108357. [CrossRef]

49. Jamshaid, M.; Rehman, A.U.; Kumar, O.P.; Iqbal, S.; Nazir, M.A.; Anum, A.; Khan, H.M. Design of dielectric and photocatalytic properties of Dy–Ni substituted $Ca_{0.5}Pb_{0.5−x}$ $Fe_{12−y}O_{19}$ M-type hexaferrites. *J. Mater. Sci. Mater. Electron.* **2021**, *32*, 16255–16268. [CrossRef]

50. Wang, J.; Guo, P.; Guo, Q.; Jönsson, P.G.; Zhao, Z. Fabrication of novel g$C_3N_4$/nanocage ZnS composites with enhanced photocatalytic activities under visible light irradiation. *CrystEngComm* **2014**, *16*, 4485–4492. [CrossRef]

51. Kolesnyk, I.; Kujawa, J.; Bubela, H.; Konovalova, V.; Burban, A.; Cyganiuk, A.; Kujawski, W. Photocatalytic properties of PVDF membranes modified with g-$C_3N_4$ in the process of Rhodamines decomposition. *Sep. Purif. Technol.* **2020**, *250*, 117231. [CrossRef]

52. Lu, X.; Wang, Q.; Cui, D. Preparation and photocatalytic properties of g-$C_3N_4$/$TiO_2$ hybrid composite. *J. Mater. Sci. Technol.* **2010**, *26*, 925–930. [CrossRef]

53. Alkhouzaam, A.; Qiblawey, H.; Khraisheh, M.; Atieh, M.; Al-Ghouti, M. Synthesis of graphene oxides particle of high oxidation degree using a modified Hummers method. *Ceram. Int.* **2020**, *46*, 23997–24007. [CrossRef]

54. Hadadian, S.; Masoudpanah, S.; Alamolhoda, S. Solution combustion synthesis of $Fe_3O_4$ powders using mixture of CTAB and citric acid fuels. *J. Supercond. Nov. Magn.* **2019**, *32*, 353–360. [CrossRef]

55. Xiao, Y.; Tian, G.; Li, W.; Xie, Y.; Jiang, B.; Tian, C.; Zhao, D.; Fu, H. Molecule self-assembly synthesis of porous few-layer carbon nitride for highly efficient photoredox catalysis. *J. Am. Chem. Soc.* **2019**, *141*, 2508–2515. [CrossRef] [PubMed]

56. Svoboda, L.; Škuta, R.; Matějka, V.; Dvorský, R.; Matýsek, D.; Henych, J.; Mančík, P.; Praus, P. Graphene oxide and graphitic carbon nitride nanocomposites assembled by electrostatic attraction forces: Synthesis and characterization. *Mater. Chem. Phys.* **2019**, *228*, 228–236. [CrossRef]